

The Effect of Wave Breaking on Surf-Zone Turbulence and Alongshore Currents: A Modeling Study*

FALK FEDDERSEN

Scripps Institution of Oceanography, La Jolla, California

J. H. TROWBRIDGE

Woods Hole Oceanographic Institution, Woods Hole, Massachusetts

(Manuscript received 13 February 2004, in final form 26 January 2005)

ABSTRACT

The effect of breaking-wave-generated turbulence on the mean circulation, turbulence, and bottom stress in the surf zone is poorly understood. A one-dimensional vertical coupled turbulence (k - ϵ) and mean-flow model is developed that incorporates the effect of wave breaking with a time-dependent surface turbulence flux and uses existing (published) model closures. No model parameters are tuned to optimize model-data agreement. The model qualitatively reproduces the mean dissipation and production during the most energetic breaking-wave conditions in 4.5-m water depth off of a sandy beach and slightly underpredicts the mean alongshore current. By modeling a cross-shore transect case example from the Duck94 field experiment, the observed surf-zone dissipation depth scaling and the observed mean alongshore current (although slightly underpredicted) are generally reproduced. Wave breaking significantly reduces the modeled vertical shear, suggesting that surf-zone bottom stress cannot be estimated by fitting a logarithmic current profile to alongshore current observations. Model-inferred drag coefficients follow parameterizations (Manning-Strickler) that depend on the bed roughness and inversely on the water depth, although the inverse depth dependence is likely a proxy for some other effect such as wave breaking. Variations in the bed roughness and the percentage of breaking-wave energy entering the water column have a comparable effect on the mean alongshore current and drag coefficient. However, covarying the wave height, forcing, and dissipation and bed roughness separately results in an alongshore current (drag coefficient) only weakly (strongly) dependent on the bed roughness because of the competing effects of increased turbulence, wave forcing, and orbital wave velocities.

1. Introduction

The mean (time averaged) bottom stress is an important component in nearshore circulation and sediment transport dynamics. In depth-integrated circulation models, the mean alongshore bottom stress τ_b^y often is written as

$$\tau_b^y = \rho c_d \langle |\mathbf{u}|v \rangle, \quad (1)$$

* Woods Hole Oceanographic Institution Contribution Number 11123.

Corresponding author address: Falk Feddersen, Scripps Institution of Oceanography, 9500 Gilman Dr., 0209, La Jolla, CA 92093-0209.
E-mail: falk@coast.ucsd.edu

where ρ is the water density, c_d is a nondimensional drag coefficient, and $\langle \rangle$ represents a time average over many wave periods. The instantaneous horizontal velocity vector \mathbf{u} and the instantaneous alongshore velocity v include both mean and wave components. To model the stress appropriately, c_d must be specified. How to parameterize c_d is still unclear. Because the bottom stress and c_d depend upon water column turbulence, both wave breaking (e.g., Fredsoe and Deigaard 1992; Church and Thornton 1993) and bed roughness (e.g., Garcez-Faria et al. 1998) have been suggested to affect c_d .

Grant and Madsen (1979) generalized the Prandtl-Karman law of the wall to the continental shelf bottom boundary layer in the presence of wave orbital velocities and bottom roughness; that is,

$$\bar{u}(z) = \frac{\bar{v}_*}{\kappa} \log\left(\frac{z}{z_a}\right), \quad (2)$$

where z is the height above the bottom, z_a is the apparent roughness height that depends on waves and on bed roughness, κ is von Kármán's constant, and the current friction velocity \bar{v}_* is defined so that

$$\tau_b^y = \rho \bar{v}_*^2. \quad (3)$$

Garcez-Faria et al. (1998) used this model to estimate the alongshore bottom stress in the nearshore (depths <4 m) by fitting a log profile (2) to alongshore current observations that spanned much of the water column, and solved for c_d using (1) and (3). Garcez-Faria et al. (1998) found that the log fit inferred c_d was inversely proportional to the fraction of waves breaking, and also that the log fit c_d was correlated ($r = 0.63$) to the root-mean-square (rms) bottom roughness normalized by water depth k_{rms}/h .

In contrast, using cross-shore integrated alongshore momentum balances, inferred surf zone c_d was roughly 3 times larger than seaward of the surf zone (Feddersen et al. 1998) and surf zone c_d was not related to k_{rms}/h (Feddersen et al. 2003). Furthermore, for two case examples, an inverse-method derived c_d was correlated with wave dissipation but not with k_{rms} or k_{rms}/h (Feddersen et al. 2004). All of these methods (log fit, momentum balances, or inverse method) for estimating c_d have problems. Development of nearshore c_d parameterizations requires resolution of the relative importance of turbulence generated by wave breaking and bed roughness to c_d .

Because turbulent motions carry the stress, this is fundamentally an issue of nearshore turbulence dynamics, where both wave breaking and near-bed shear generate turbulence. In the open ocean, wave breaking results in an enhanced (i.e., >production) near-surface dissipation layer (e.g., Agrawal et al. 1992) that extends to many times the wave height (Kitaigorodskii et al. 1983). However, the surf zone is usually no more than a few wave heights deep, and thus both open-ocean breaking wave and near-bed boundary layer regimes overlap. Breaking-wave-generated turbulence can affect the near-bed region (Voulgaris and Collins 2000; Cox and Kobayashi 2000), and in the laboratory, near-surface grid-generated turbulence even can influence the wave boundary layer (Fredsoe et al. 2003). However, in 4.5-m mean depth, 1 m above the bed, no enhanced dissipation (i.e., dissipation equaled production) was observed under breaking waves (Trowbridge and Elgar 2001), in contrast to the open-ocean results (e.g., Agrawal et al. 1992).

To examine these issues, a one-dimensional (1D) vertical mean flow and turbulence model is developed (section 2) that incorporates the effect of breaking-wave-generated turbulence through a time-dependent surface flux extending the steady approach often used in open-ocean modeling (Craig and Banner 1994; Burchard 2001). Model parameters are constrained by the literature and are not tuned to improve model–data agreement. Detailed and quantitative model–data agreement is not the goal. Instead, qualitative agreement with both the observed mean alongshore current and dissipation is sought, which allows the effects of breaking-wave-generated turbulence on the surf-zone hydrodynamics to be examined. The model is tested with two case examples. The first (section 3) is the most energetic case reported by Trowbridge and Elgar (2001)—the only published combined mean-flow, stress, and dissipation field measurements in the near shore. To further test the model dissipation predictions, a nondimensional scaling is developed that collapses two independent surf-zone dissipation datasets (section 4). These nondimensionalized dissipation observations are used to test the model (section 5) using a well-studied Duck94 case example (e.g., Garcez-Faria et al. 1998; Feddersen et al. 2004) where only currents were observed. The model with a breaking-wave turbulence source reproduces the observed dissipation depth dependence and slightly underpredicts the alongshore current.

The model results are then used to investigate the effect of wave breaking and bed roughness on water-column turbulence, alongshore currents, and the drag coefficient. Wave breaking decreases significantly the vertical shear of the alongshore current, consequently log fit–inferred bed-shear stress and c_d are biased low (section 6a). Existing parameterizations for c_d that depend on bed roughness and water depth are investigated (section 6b). Numerical experiments with varying bed roughness and breaking-wave inputs are used to determine the relative importance of each to the alongshore current and c_d (section 7). The results are summarized in section 8.

2. Model

a. Model equations

A right-handed coordinate system is used where x is the cross-shore coordinate, increasing offshore with origin ($x = 0$) at the shoreline where the mean water depth $h = 0$, y is the alongshore coordinate, and the vertical coordinate z increases upward with origin at the seabed. The water density ρ is constant and the effects of rotation are neglected. The turbulence and currents are

represented by a depth- and time- (t) dependent model with a fixed free surface and no net vertical velocities. Although vertical wave velocities can be strong near the surface in the surf zone, the model is intended to represent turbulence and current processes below trough level.

The equations for the cross-shore u and alongshore v velocities are

$$\begin{aligned}\frac{\partial u}{\partial t} &= \frac{\partial}{\partial z} \left(K_v \frac{\partial u}{\partial z} \right) + F_x \quad \text{and} \\ \frac{\partial v}{\partial t} &= \frac{\partial}{\partial z} \left(K_v \frac{\partial v}{\partial z} \right) + F_y,\end{aligned}$$

where F_x and F_y represent specified time-dependent depth uniform cross- and alongshore sinusoidal wave forcing with period T . For a given root-mean-square (rms) wave height H_{rms} and wave angle θ in water depth h , the (zero mean) oscillatory wave forcing is the instantaneous pressure gradient induced by a progressive sinusoidal shallow water wave, that is,

$$(F_x, F_y) = \frac{\pi g H_{\text{rms}}}{T \sqrt{gh}} \cos(2\pi t/T) \times [\cos(\theta), \sin(\theta)]. \quad (4)$$

Note that, in model–data comparisons, the sinusoidal orbital wave forcing is chosen so that the forcing variance is equivalent to that that would result from a random wave field with observed H_{rms} . The vertical eddy viscosity K_v is specified through the turbulence model. Advective terms (e.g., $u\partial_x$) are not considered. No-slip boundary condition for u and v are applied at the bed $z = 0$. At the surface $z = h$, the boundary conditions $K_v \partial u / \partial z = 0$ and $K_v \partial v / \partial z = \bar{v}_{*s}^2$ are applied where \bar{v}_{*s}^2 is the alongshore surface stress. Following Deigaard (1993), the mean alongshore wave forcing is applied as a steady surface stress (appendix A) so that the surface stress is the sum of wind and wave forcing,

$$\bar{v}_{*s}^2 = \rho^{-1} \left(\tau_y^w - \frac{dS_{xy}}{dx} \right), \quad (5)$$

where τ_y^w is the alongshore wind stress, and dS_{xy}/dx is the radiation stress gradient. Thus the modeled water column is a (time-averaged) constant stress layer. Mean cross-shore wave forcing is not included (appendix A).

The turbulence is modeled with the k - ε equations (e.g., Rodi 1987), used in a variety of engineering and geophysical fluid dynamics problems. The equation for the turbulent kinetic energy (TKE) k consists of contributions due to turbulence diffusion, shear production, and dissipation; that is,

$$\frac{\partial k}{\partial t} = \frac{\partial}{\partial z} \left(K_v \frac{\partial k}{\partial z} \right) + K_v S^2 - \varepsilon, \quad (6)$$

where the shear production $P = K_v S^2$, S^2 is the total squared shear, that is,

$$S^2 = \left(\frac{\partial u}{\partial z} \right)^2 + \left(\frac{\partial v}{\partial z} \right)^2,$$

and ε represents the dissipation of TKE. The equation for the dissipation ε is

$$\frac{\partial \varepsilon}{\partial t} = \frac{\partial}{\partial z} \left(\frac{K_v}{\sigma_\varepsilon} \frac{\partial \varepsilon}{\partial z} \right) + \frac{\varepsilon}{k} (c_{1\varepsilon} P - c_{2\varepsilon} \varepsilon),$$

where $c_{1\varepsilon}$ and $c_{2\varepsilon}$ are constants (section 2c). The possible effects of bubble-generated buoyancy fluxes are not considered. The vertical eddy viscosity K_v for momentum and TKE are identical; however, the vertical eddy viscosity for dissipation is modified by a dissipation Schmidt number σ_ε (section 2c). In the k - ε model, the vertical eddy viscosity for momentum and TKE is

$$K_v = C_\mu^4 \frac{k^2}{\varepsilon}, \quad (7)$$

where C_μ is a function of the nondimensionalized shear $\alpha_M = k^2 S^2 / \varepsilon^2$ (Canuto et al. 2001; Burchard 2001)

$$C_\mu^4 = \frac{0.107 - 0.00012\alpha_M}{1 + 0.02872\alpha_M - 0.000034\alpha_M^2}. \quad (8)$$

The turbulence length scale l is related to k and ε by the standard relation

$$l = (C_\mu^0)^3 k^{3/2} / \varepsilon, \quad (9)$$

where $(C_\mu^0)^4 = 0.107$ (i.e., $C_\mu \rightarrow C_\mu^0$ as $\alpha_M \rightarrow 0$).

The bottom boundary conditions for k and ε are derived by assuming a near-bottom balance between production and dissipation (Mellor and Yamada 1982) and a bottom turbulent length scale $l = \kappa z_{0b}$ where $\kappa = 0.4$ is von Kármán's constant and z_{0b} is the (specified) hydrodynamic bed roughness. The hydrodynamic bed roughness z_{0b} is related to the physical roughness k_{rms} by the Nikuradse (1933) relation $z_{0b} = k_{\text{rms}}/30$. Using (7) and (9), the near-bed TKE production–dissipation balance becomes (for small α_M)

$$C_\mu^0 (\kappa z_{0b}) k_b^{1/2} S^2 = (C_\mu^0)^3 \frac{k_b^{3/2}}{\kappa z_{0b}},$$

where k_b is the near-bed TKE, resulting in

$$k_b = (C_\mu^0)^{-2} (\kappa z_{0b})^2 S^2,$$

which is identical to the log-layer bottom boundary condition $k_b = u_*^2 / (C_\mu^0)^2$. The ε bottom boundary condition becomes

$$\varepsilon = (C_\mu^0)^3 \frac{k_b^{3/2}}{\kappa z_{0b}}.$$

b. Breaking-wave turbulence sources

Turbulence in the open-ocean under breaking waves has been modeled using a steady surface flux of TKE (e.g., Craig and Banner 1994; Terray et al. 1999; Burchard 2001), that is,

$$K_v \frac{\partial k}{\partial z} = \bar{\epsilon}_w \quad (10)$$

at $z = h$, where $\bar{\epsilon}_w$ is the downward TKE flux due to breaking waves. By assuming a well-developed sea where the energy input by the wind balances that dissipated by wave breaking, $\bar{\epsilon}_w$ is related to the wind friction velocity cubed. Such models have success in predicting enhanced dissipation in the surface layer (Craig and Banner 1994) and in reproducing (Terray et al. 1999; Burchard 2001) the observed open-ocean dissipation depth scaling (Anis and Moum 1995; Terray et al. 1996; Drennan et al. 1996).

In contrast, in the surf zone the cross-shore gradient of onshore wave energy flux \mathcal{F}_x supplies turbulence to the water column; that is, for an alongshore uniform beach $d\mathcal{F}_x/dx = \bar{\epsilon}_w$, which is estimated either by cross-shore differencing \mathcal{F}_x measurements (e.g., Elgar et al. 1997; Trowbridge and Elgar 2001) or from a wave transformation model (e.g., Thornton and Guza 1983). The details of the breaking-wave turbulence source likely depend on whether wave breaking is initiating as a plunging or spilling wave, or is a self-similar bore (i.e., constant H_{rms}/h). For initiating-breaking spilling waves and for bores, a surface TKE flux boundary condition is likely a reasonable representation of how the turbulence enters the water column. Intense plunging surf-zone waves almost instantaneously deliver turbulence throughout the entire water column suspending sediment (Voulgaris and Collins 2000), and a flux boundary condition is likely inappropriate. However, intense plunging waves are rapidly transformed into self-similar bores, so the cross-shore region where this is inappropriate is arguably small.

Wave energy is the sum of two components: potential and kinetic energy. As waves break, a portion of the dissipated wave energy goes into TKE, but a portion also goes into turbulent potential energy by entraining bubbles into the water column. The work required to entrain air into the water column can account for 30%–50% (or higher) of the dissipated wave energy (Lamarre and Melville 1991). Wave energy also goes into creation of a wave roller (Duncan 1981; Svendsen 1984). Some of this energy is dissipated in the wave roller and some is turbulently diffused into the water column. Thus only a fraction of the dissipated wave energy is fluxed as turbulence into the water column. Assuming

one-half of the wave energy goes into TKE and one-half of that is dissipated in the roller, the model allows 25% of the wave energy dissipation ($\bar{\epsilon}_w/4$) to diffuse into the water column as TKE. The effect of varying this percentage is discussed further in section 6b.

The time dependence associated with breaking is not captured by a steady surface TKE flux boundary condition, and the nonlinear time-dependent response of the turbulence and dissipation can differ from the steady response (appendix B). The time dependence of the wave breaking in the surf zone is captured by idealizing the surface boundary condition so that breaking waves pass by every wave period T supplying a delta function flux of turbulence; that is,

$$K_v \frac{\partial k}{\partial z} = \frac{\bar{\epsilon}_w T}{4} \delta(t - nT), \quad (11)$$

resulting in a time-averaged TKE flux of $\bar{\epsilon}_w/4$. Numerically the delta function in (11) is implemented as a top-hat function with a width of about 1 s. Note that the time dependence in the TKE surface boundary condition (11) is in contrast to the steady surface-stress boundary condition for v (5). As a second hypothesis that breaking-wave-generated turbulence is not important to surf-zone turbulence dynamics, a zero-TKE-flux surface boundary condition is also examined,

$$K_v \frac{\partial k}{\partial z} = 0. \quad (12)$$

The model with the surface TKE flux (11) or no surface TKE flux (12) is hereinafter denoted as breaking and nonbreaking configurations, respectively.

The surface boundary condition for ϵ is a Dirichlet boundary condition where ϵ is related to k through a surface mixing length scale z_{0s} (analogous to a bed roughness)

$$\epsilon = (C_\mu^0)^3 \frac{k^{3/2}}{\kappa z_{0s}}, \quad \text{at } z = h.$$

The required specification of z_{0s} is discussed in section 2c.

c. Model coefficients and closures

The model parameters $c_{1\epsilon}$, $c_{2\epsilon}$, σ_ϵ , and z_{0s} remain to be specified. In decaying homogeneous turbulence $c_{2\epsilon}$ is constrained by the turbulence decay rate d ; that is, $k \sim t^{-d}$ so that $d = (c_{2\epsilon} - 1)^{-1}$ (e.g., Reynolds 1976). The standard value $c_{2\epsilon} = 1.92$ (Rodi 1987) yields $d = 1.1$, a value in line with observed homogeneous turbulence decay rates (Reynolds 1976; Tennekes 1989; Mohamed and Larue 1990) and is also consistent with the observed t^{-1} TKE decay rate after laboratory wave-break-

ing events (Rapp and Melville 1990; Melville et al. 2002). The requirement that the mean shear not impose a length scale in homogeneous shear flow results in $c_{1\varepsilon} = 3/2$ (Tennekes 1989), close to the experimentally derived standard value of $c_{1\varepsilon} = 1.44$ (Rodi 1987), which is used here.

In a turbulent logarithmic boundary layer, production balances dissipation. However, for ε to remain in steady state, the excess dissipation of ε (because $c_{2\varepsilon} > c_{1\varepsilon}$) must be balanced by ε diffusion resulting in a σ_ε constraint (e.g., Umlauf and Burchard 2003),

$$\sigma_\varepsilon = \frac{\kappa^2}{C_\mu^2(c_{2\varepsilon} - c_{1\varepsilon})},$$

which yields $\sigma_\varepsilon = 1.07$ for weak shear ($C_\mu \rightarrow C_\mu^0$ for small α_M). Shear-free diffusion of TKE away from a grid where diffusion balances dissipation is another constraint on σ_ε . Solutions based on $\varepsilon = \varepsilon_0 \hat{z}^a$ and $l = l_0 \hat{z}$ where \hat{z} is the distance from the grid and with $\sigma_\varepsilon = 1.07$ result in far too large decay power $a = -49$ (Umlauf and Burchard 2003) when compared with the observed open ocean $\varepsilon \sim \hat{z}^{-2}$ depth scaling (Terray et al. 1996). To reproduce the Terray et al. (1996) ε scaling requires $\sigma_\varepsilon \approx 2.6$. Because the surf zone is a region with both bottom boundary layer shear-produced turbulence and breaking-wave-generated turbulence, following Burchard (2001), σ_ε is made a linear function of P/ε so that for $P/\varepsilon = 1$ the logarithmic bottom boundary layer σ_ε is taken, and for $P/\varepsilon = 0$ the limiting value is $\sigma_\varepsilon = 2.4$ [based on analytic solutions of Craig (1996), $\varepsilon \sim \hat{z}^{-2.68}$]. With this σ_ε in the k - ε model, Burchard (2001) reproduced the observed open-ocean ε scaling (Anis and Moum 1995; Terray et al. 1996; Drennan et al. 1996).

In turbulence models under open-ocean breaking waves, z_{0s} is of the order of the wave height (e.g., Craig and Banner 1994; Burchard 2001). In particular, with z_{0s}/H_{rms} between 0.35 and 1.4, the scaled near-surface open-ocean ε scaling is reproduced (Burchard 2001), although the model upper boundary begins at a depth of z_{0s} , leaving an unresolved surface layer of thickness order the wave height. In the surf zone this would consume a good portion of the water column. A second possibility for z_{0s} was discussed by Gemmrich and Farmer (1999) who examined the vertical extension of near-surface temperature fluctuations and found the surface mixing length scale $z_{0s} = 0.2$ m for (white capping) rms wave heights of 2–3.5 m, much smaller than the z_{0s} values previously used in modeling. In the next section, the two possibilities for z_{0s} suggested by the literature, 1) $z_{0s}/H_{\text{rms}} = 0.5$ (Burchard 2001) and 2) $z_{0s} = 0.2$ m (Gemmrich and Farmer 1999), are examined to determine which value is more appropriate for surf-zone turbulence modeling.

3. Surf-zone case example from Trowbridge and Elgar (2001)

Trowbridge and Elgar (2001) report the only set of published simultaneous nearshore field measurements of mean currents, shear, stress, and dissipation under breaking waves. Their nearshore turbulence observations made at Duck, North Carolina, approximately 300 m from the shoreline in roughly 4.5-m water depth, 1 m above the bed, occasionally were in the surf zone. Wave dissipation $\bar{\varepsilon}_w$ was estimated by cross-shore differencing wave energy flux observations. During periods of wave breaking, the depth-normalized wave dissipation $\bar{\varepsilon}_w/h$ was $O(10^2)$ larger than the observed mean¹ dissipation $\bar{\varepsilon}$, leading Trowbridge and Elgar (2001) to conclude that most TKE dissipation occurred near the surface. During these periods of wave breaking, the observed shear production balanced dissipation. No enhanced $\bar{\varepsilon}$ was observed, in contrast with open ocean observations that indicate enhanced $\bar{\varepsilon}$ at depths a few times the wave height (e.g., Agrawal et al. 1992).

The model is tested using the largest breaking-wave (and $\bar{\varepsilon}$) conditions observed by Trowbridge and Elgar (2001) yearday 291.7, when their instruments were within the surf zone. The conditions are $h = 4.8$ m, $H_{\text{rms}} = 1.74$ m, and $T = 6$ s (estimated as 1 over the energy-weighted mean frequency). The oscillating wave forcing (F_x and F_y) is calculated from (4) using the observed H_{rms} , wave period and angle, and water depth. The water side alongshore wind friction velocity $\bar{v}_*^w = 0.024$ m s⁻¹. Based on differencing wave observations, $\bar{\varepsilon}_w = 9.9 \times 10^{-2}$ m³ s⁻³ and the mean alongshore forcing due to radiation stress gradients is $\rho^{-1} dS_{xy}/dx = -1.9 \times 10^{-3}$ m² s⁻², applied as a surface stress (section 2a). The physical bed roughness was not observed. However, at this distance from the shoreline, values of 1–2 cm are typical (Thornton et al. 1998; Gallagher et al. 2003; Feddersen et al. 2003) and so $z_{0b} = 0.015$ m/30 = 5×10^{-4} m is used. The model results are not sensitive to factor 2 variations in bed roughness. To examine the effects of breaking-wave-injected turbulence on the mean flow and turbulence, the model is run for these conditions in the breaking (11) and nonbreaking (12) configurations. The breaking runs are performed with both surface mixing lengths candidates, $z_{0s} = 0.2$ m (resulting in $z_{0s}/H_{\text{rms}} = 0.11$) and $z_{0s} = H_{\text{rms}}/2 = 0.88$ m. The model simulations are run until equilibrated and results are

¹ The observed dissipations here and in the next section are considered representative of the mean dissipation because they are based on fluid velocity statistics averaged over many wave periods.

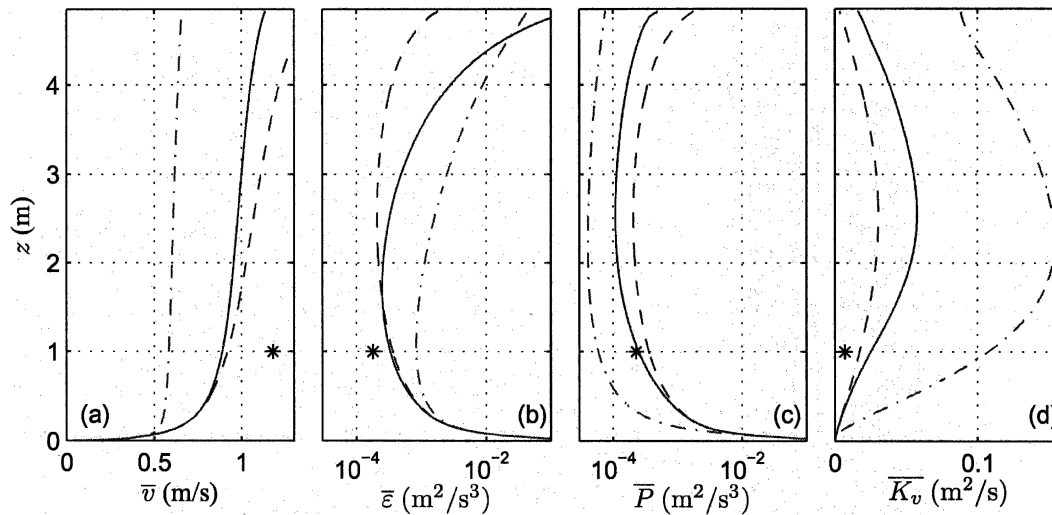


FIG. 1. Depth profiles of (a) mean alongshore current \bar{v} , (b) mean dissipation $\bar{\epsilon}$, (c) mean production \bar{P} , and (d) mean eddy viscosity \bar{K}_v for the Trowbridge and Elgar (2001) yearday 291.7 observations (*), modeled nonbreaking with $z_{0s} = 0.2$ m (dashed), breaking with $z_{0s} = 0.2$ m (solid), and breaking with $z_{0s} = H_{rms}/2 = 0.88$ m (dash-dot). The observed \bar{K}_v is estimated by $\bar{K}_v = \langle v'w' \rangle / (d\bar{v}/dz)$.

shown with the observations in Fig. 1 and summarized in Table 1.

The breaking run with $z_{0s} = H_{rms}/2$ (dash-dot curve in Fig. 1) results in mean alongshore current \bar{v} that is one-half of that observed, and modeled mean dissipation $\bar{\epsilon}$ and \bar{P} that are larger and much smaller, respectively, than observed (asterisks in Fig. 1). The modeled mean \bar{K}_v is larger than the other runs resulting in much larger diffusion of turbulence throughout the water column and a large reduction in the \bar{v} vertical shear. This is in contrast to the breaking $z_{0s} = 0.2$ m and nonbreaking runs (solid and dashed curves in Fig. 1) where the modeled \bar{v} is within 0.25 m s^{-1} of the observed, and production and dissipation balance and are within a factor of 2 of the observation (Table 1). Based on these (and subsequent) runs, the use of the surface mixing length $z_{0s} = H_{rms}/2$ is inappropriate in this case and only the model runs with $z_{0s} = 0.2$ m are discussed further.

At the level of the observation (1 m above the bed), little difference in \bar{v} and turbulence quantities exists between the nonbreaking and breaking configuration with $z_{0s} = 0.2$ m, and neither configuration is preferable. There are also uncertainties in the wave forcing and energy flux gradients and potential errors in the estimates of observed $\bar{\epsilon}$ and \bar{P} . Higher in the water column ($z > 2$ m), the breaking-wave surface TKE flux increases the dissipation (resulting in $\bar{\epsilon} > \bar{P}$) and the eddy viscosity (Figs. 1b,d). Because of the constant stress, the shear is reduced (Fig. 1a). The nonbreaking $\bar{\epsilon}$ also increases (although weakly) near the surface (dashed curve in Fig. 1b) because, although TKE is

constant with depth, the length scale decreases toward the surface.

The breaking configured model result suggests that the reason Trowbridge and Elgar (2001) observed an $\bar{\epsilon} = \bar{P}$ balance under breaking waves, when in the open ocean enhanced dissipation ($\bar{\epsilon} > \bar{P}$) is observed to depths many times the wave height (Agrawal et al. 1992), is because the observations are under the influence of the bottom boundary layer. Within the bottom 1.5 m, the modeled $\bar{\epsilon}$ scales as z^{-1} , decreasing with height above the bed as appropriate for the bottom boundary layer. According to the model, if the water were deeper or the instrument location higher, en-

TABLE 1. Observed and modeled current and turbulence values 1 m above the bed for the Trowbridge and Elgar (2001) case example. The model is run in breaking and nonbreaking configurations with surface mixing lengths of $z_{0s} = 0.2$ m (Gemrich and Farmer 1999) and breaking configuration with $z_{0s} = H_{rms}/2 = 0.88$ m (Burchard 2001). The observed \bar{K}_v is estimated by $\bar{K}_v = \langle v'w' \rangle / (d\bar{v}/dz)$.

| | \bar{v} (m s^{-1}) | $\bar{\epsilon}^*$ | \bar{P}^* | $\frac{d}{dz} \left(\bar{K}_v \frac{d\bar{v}}{dz} \right)^*$ | \bar{K}_v ($\text{m}^2 \text{s}^{-1}$) |
|-------------|------------------------------------|--------------------|-------------|---|---|
| | Observed | | | | |
| | 1.18 | 1.8 | 2.3 | — | 0.7×10^{-2} |
| | $z_{0s} = 0.2$ m | | | | |
| Breaking | 0.89 | 3.3 | 2.5 | 0.8 | 2.5×10^{-2} |
| Nonbreaking | 0.92 | 3.6 | 3.6 | 0.0 | 1.7×10^{-2} |
| | $z_{0s} = H_{rms}/2 = 0.88$ m | | | | |
| Breaking | 0.58 | 8.3 | 0.6 | 7.7 | 11×10^{-2} |

* Units: $\times 10^{-4} \text{ m}^2 \text{ s}^{-3}$.

hanced dissipation would have been observed. This also explains why so little dissipation was observed relative to the depth-normalized flux, $\bar{\epsilon}_w/h$.

4. Surf-zone dissipation observations and scaling

In addition to Trowbridge and Elgar (2001), there are two other sets of surf-zone field dissipation observations. Using a hot-film anemometer in the surf zone at La Jolla, California, George et al. (1994) estimated $\bar{\epsilon}$ at different wave heights and water depths. Bryan et al. (2003), using an acoustic Doppler velocimeter (ADV) on two beaches in New Zealand [with generally smaller waves and shallower depths than George et al. (1994)], found $\bar{\epsilon}$ magnitudes smaller than those of George et al. (1994). Both George et al. (1994) and Bryan et al. (2003) measured only $\bar{\epsilon}$ and not other turbulence quantities such as shear production, nor were the conditions required for model input (e.g., $\bar{\epsilon}_w$) measured. To compare these two $\bar{\epsilon}$ datasets with each other and with model predictions, a nondimensionalization of surf-zone dissipation is developed.

In a self-similar surf zone (where $H_{\text{rms}} = \gamma h$ and $c_g = \sqrt{gh}$) the cross-shore wave energy flux becomes (for normally incident waves)

$$\mathcal{F}_x = \frac{1}{8} g H_{\text{rms}}^2 c_g = \frac{1}{8} g^{3/2} \gamma^2 h^{5/2},$$

and results in (for a planar beach with slope $\beta = dh/dx$) a (time-averaged) surface TKE flux of

$$\frac{\bar{\epsilon}_w}{4} = \frac{5}{64} g^{3/2} \gamma^2 h^{3/2} \beta$$

and a depth-mean dissipation of

$$\bar{\epsilon} = \frac{\bar{\epsilon}_w}{4h} = \frac{5}{64} \gamma^2 \beta \sqrt{g^3 h}.$$

Therefore, nondimensionalized surf-zone $\bar{\epsilon}/(g^3 h)^{1/2}$ observations should result in scaled values around $(5/64)\gamma^2\beta$. With γ typically varying between 0.3 to 0.9 (Raubenheimer et al. 1996) and β between 0.02 and 0.06, $(5/64)\gamma^2\beta$ ranges between 1.5 and 38 ($\times 10^{-4}$). A similar nondimensionalization is derived if $\bar{\epsilon}$ is nondimensionalized by u^3/l using $(gh)^{1/2}$ and h for u and l , respectively (George et al. 1994), although this cannot explain the magnitude of the nondimensional dissipation.

The nondimensional $\bar{\epsilon}$ observations of Bryan et al. (2003) and George et al. (1994) overlap (Fig. 2), indicating that, although the depths and wave heights varied, a comparable fraction of wave dissipation was ob-

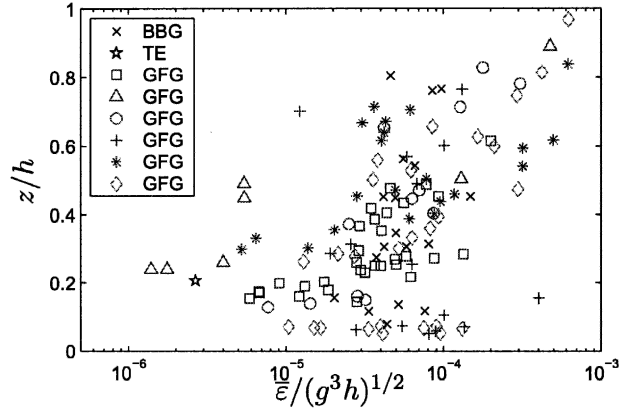


FIG. 2. Nondimensionalized surf zone dissipation $\bar{\epsilon}/(g^3 h)^{1/2}$ observations of Bryan et al. (2003) (BBG: crosses), Trowbridge and Elgar (2001) (TE: star), and George et al. (1994) (RG: remainder of symbols) as a function of normalized height above the bed z/h . The George et al. (1994) data are from their Fig. 6, and the Bryan et al. (2003) observations are restricted to those in the surf zone.

served by both. In the heart of the water column, the observed $\bar{\epsilon}/(g^3 h)^{1/2}$ mostly range between 3 and 30 ($\times 10^{-5}$), which is about a factor of 10 less than $(5/64)\gamma^2\beta$ range [much less than the factor of 100 smaller reported by Trowbridge and Elgar (2001); star in Fig. 2], suggesting that a significant amount [relative to Trowbridge and Elgar (2001)] of the total wave dissipation was observed by George et al. (1994) and Bryan et al. (2003). Bryan et al. (2003) also report beach slope β and mean wave frequency from which γ are estimated (Raubenheimer et al. 1996). Fully normalizing their dissipation observations results in $\bar{\epsilon}/[(5/64)\beta\gamma^2(g^3 h)^{1/2}]$ value between 0.15 and 1.7, further indicating that Bryan et al. (2003) observed a significant portion of the breaking-wave dissipation. In general, the observed $\bar{\epsilon}/(g^3 h)^{1/2}$ increase toward the surface through most of the water column, indicating that the dominant source of turbulence is due to wave breaking and that $\bar{\epsilon} > \bar{P}$. In the lower 20% of the water column, the observed $\bar{\epsilon}/(g^3 h)^{1/2}$ roughly increase toward the bed as expected in a traditional turbulent boundary layer (i.e., $\bar{\epsilon} = \bar{P}$). The Trowbridge and Elgar (2001) case example $\bar{\epsilon}/(g^3 h)^{1/2} = 2.7 \times 10^{-6}$ (star in Fig. 2) at $z/h = 0.21$ is weak relative to the other observations, further indicating that the turbulence dynamics in this case example are dominated by bottom boundary layer processes.

5. Duck94 case example

The Trowbridge and Elgar (2001) case example used to test the model was in relatively deep water for the surf zone and (according to the model) the observations

were too deep to determine whether breaking-wave-generated turbulence was important throughout the water column. Unfortunately there are no other field surf-zone wave, mean flow, and turbulence observations to test the model. George et al. (1994) and Bryan et al. (2003) report only dissipation observations and not the necessary model inputs to simulate their observations. Instead the model is tested with an alongshore uniform (Feddersen et al. 1998; Ruessink et al. 2001) case example (Feddersen et al. 2004) from the Duck94 field experiment, comparing the mean \bar{v} observations with the model. Both cross-shore transect and a single vertical profile \bar{v} data are included in the comparison. Because turbulence quantities were not measured, the modeled case-example dissipation is compared with existing nondimensionalized surf-zone dissipation observations (section 4).

a. Duck94 case example conditions

In the Duck94 case example (1700 EST 10 October 1994), wave breaking begins offshore of the bar crest located at $x = 110$ m (Figs. 3a,b). A tuned 1D wave model (e.g., Thornton and Guza 1983) accurately (rms error 2 cm) predicts the wave height evolution (solid curve in Fig. 3b), and the roller model (e.g., Ruessink et al. 2001) predicts $\bar{\epsilon}_w$ (Fig. 3c) for the surface TKE flux boundary condition (11). The wave-roller model (initialized with offshore H_{rms} and S_{xy} estimated from an array of pressure sensors in 8-m water depth), together with wind stress observations, gives the mean alongshore forcing \bar{v}_{*s}^2 (5) applied as a surface stress (Fig. 3d). Bed roughness k_{rms} , observed at fixed altimeters (see Gallagher et al. 1998; Feddersen et al. 2003 for details), ranged between 1 and 7 cm with generally larger values in the bar trough and near the shoreline (Fig. 3e). All but one of the sensor locations in Fig. 3e have a single current meter. The cross-shore location at $x = 21$ m, second closest to shore, has a vertical stack of four current meters ranging from 0.35 to 1.4 m above the bed (10 October run 7; Garcez-Faria et al. 1998). At this location, k_{rms} was interpolated between the adjacent observations (circle in Fig. 3e).

These inputs (together with the Snell's law derived wave angle and wave period $T = 6$ s) are used to drive the model at the 12 current-meter locations (symbols in Figs. 3b,c) subdivided into four regions: the foreshore and the bar crest both with active wave breaking $\bar{\epsilon}_w \geq 0.023 \text{ m}^3 \text{ s}^{-3}$, the bar trough with some wave roller dissipation $0.008 \leq \bar{\epsilon}_w < 0.023 \text{ m}^3 \text{ s}^{-3}$, and seaward of the surf zone with weak wave roller dissipation $\bar{\epsilon}_w < 0.006 \text{ m}^3 \text{ s}^{-3}$. Both the breaking and nonbreaking model configurations are run to determine which provides a better fit to the observations. The surface mixing length z_{0s}

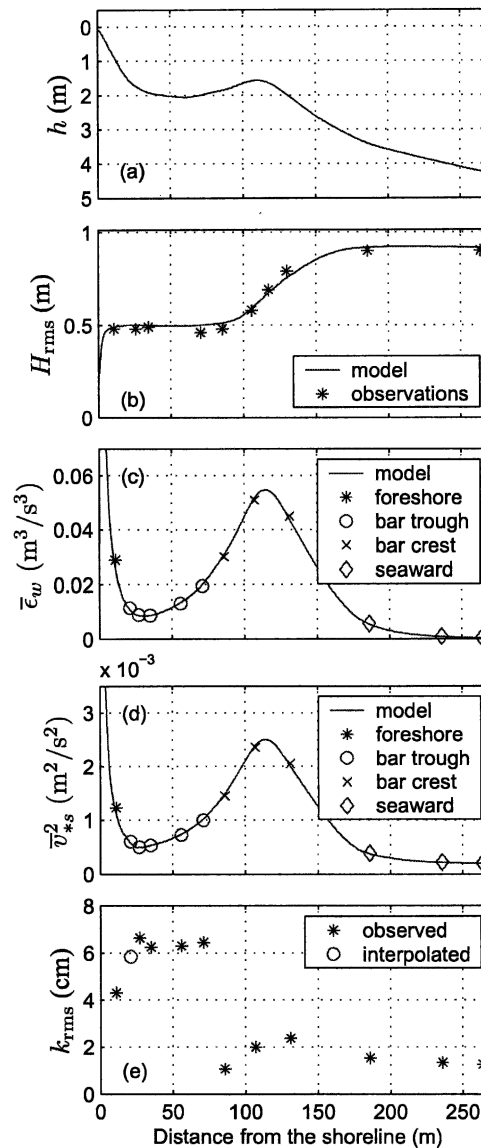


FIG. 3. Duck94 conditions (1700 EST 10 Oct 1994) vs distance from the shoreline: (a) depth h , (b) model (solid) and observed (asterisks) H_{rms} , (c) roller-model-derived $\bar{\epsilon}_w$, (d) alongshore (wave + wind) surface stress \bar{v}_{*s}^2 (5), and (e) observed (asterisks) and interpolated (circles) k_{rms} . The symbols in (c) and (d) represent the 12 current-meter locations and are subdivided into four regions: foreshore ($x \leq 20$ m, asterisk), bar trough ($25 < x \leq 75$ m, circles), bar crest ($80 < x \leq 130$ m, crosses), and seaward of the surf zone ($x > 170$ m, diamonds) as noted in the legend. The most onshore bar trough (circle) location is where the vertical profile \bar{v} data (10 Oct run 7; Garcez-Faria et al. 1998) were taken and has interpolated k_{rms} in (e). There are only 10 wave observations.

$= 0.2$ m is used at all locations resulting in z_{0s}/H_{rms} varying between 0.21 and 0.43. Model runs with either $z_{0s}/H_{rms} = 0.5$ or $z_{0s}/H_{rms} = 0.11$ (used in section 3) give significantly degraded results relative to $z_{0s} = 0.2$ m.

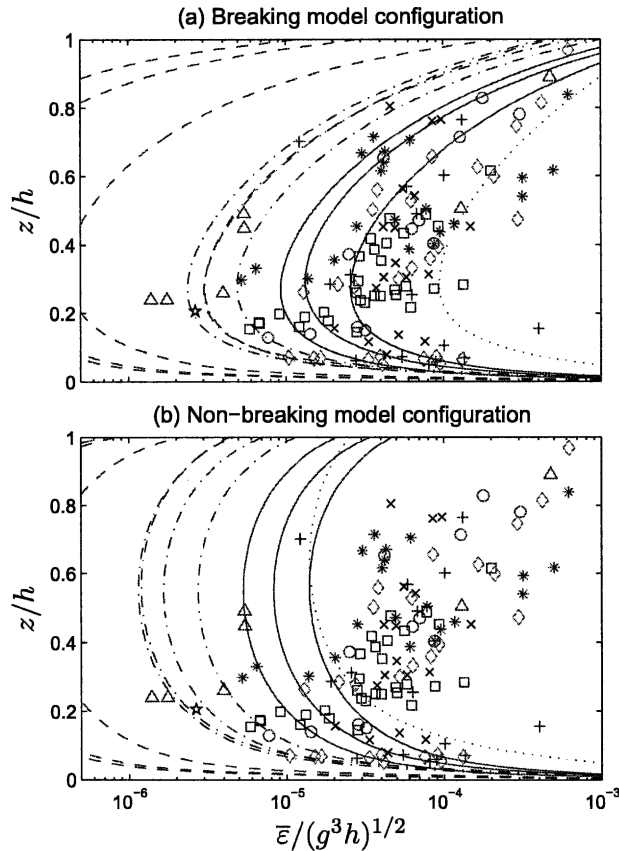


FIG. 4. Modeled Duck94 case example nondimensionalized dissipation $\bar{\epsilon}/(g^3 h)^{1/2}$ profiles as a function of normalized height above the bed (z/h) with (a) breaking (11) and (b) nonbreaking (12) model configurations. The modeled curves are for the fore-shore (dotted), bar trough (dash-dot), bar crest (solid), and seaward of the surf zone (dashed) current-meter locations (Fig. 3). The symbols are the nondimensional surf-zone dissipation observations shown in Fig. 2.

b. Duck94 case example model–data comparison

With the breaking configuration (11), the nine modeled surf-zone ($x < 130$ m) nondimensional dissipation $\bar{\epsilon}/(g^3 h)^{1/2}$ profiles follow the observed surf-zone dissipation scaling (solid, dotted, and dash-dot curves in Fig. 4a). The three locations seaward of the surf zone, with small $\bar{\epsilon}_w$, have dissipation profiles (dashed curves in Fig. 4a) that are orders of magnitude smaller than the observed nondimensionalized surf-zone dissipation. The foreshore location with depth 0.8 m has the largest nondimensional $\bar{\epsilon}$ profile (dotted curve). The three bar crest locations (solid curves) with active wave breaking most closely follow the nondimensional $\bar{\epsilon}$ observations. The five bar trough locations (dash-dot curves) have weaker $\bar{\epsilon}/(g^3 h)^{1/2}$ because in this region without active breaking the self-similar scaling of $H_{\text{rms}} = \gamma h$ is inappropriate. Most of the modeled nondimensional $\bar{\epsilon}$ have

a minimum near $z/h = 0.25$, which is the transition point where the turbulence dynamics shift from dissipation balancing TKE diffusion above (i.e., enhanced dissipation $\bar{\epsilon} \gg \bar{P}$) to balancing shear production below (i.e., $\bar{\epsilon} = \bar{P}$ in the current boundary layer). This minimum nondimensional $\bar{\epsilon}$ also can be discerned in the observed $\bar{\epsilon}/(g^3 h)^{1/2}$ (Figs. 2 and 4).

In contrast, with the nonbreaking model configuration (12), the nine surf-zone modeled nondimensionalized mean dissipation profiles do not match the observed dissipation scaling through the upper 2/3 of the water column. Near the bed (bottom 20%), the $\bar{\epsilon}/(g^3 h)^{1/2}$ profiles with and without wave breaking are similar (because $\bar{\epsilon} = \bar{P}$ in the current boundary layer) and largely match the observations. The improved predictions with the breaking configuration strongly suggest that breaking-wave-generated turbulence cannot be neglected in modeling surf-zone water-column hydrodynamics.

However, the breaking model configuration does not lead to overall improvements over the nonbreaking model configuration in \bar{v} model predictions (Fig. 5, lower panel) at the instrument locations. The rms errors are 0.15 and 0.11 m s^{-1} for the breaking and nonbreaking configurations, respectively. This level of agreement is encouraging because no tuning of model parameters has been performed and some physics (e.g., lateral mixing) has been neglected. Similar to the Trowbridge and Elgar (2001) case example (section 3) both model configurations tend to underpredict the observed \bar{v} (Fig. 5, lower panel), particularly between $x = 75$ and $x = 110$ m where wave breaking is strongest (Figs. 3b,c), suggesting that either the wave-model-derived forcing is in error or that the model is too frictional. Tuning model parameters (e.g., decreasing bed roughness) would improve model predictions.

It is also of interest to compare modeled \bar{v} vertical structure with observations (Fig. 5, top panels). Most \bar{v} observations were made between 0.4 and 0.7 m above the bed, where typically $z/h \leq 0.25$. Because of the influence of the seabed, at this height no substantial difference between the breaking and nonbreaking model predictions is usually observed. Farther up in the water column at the surf-zone locations (1–8), the breaking configured runs have a much reduced shear $d\bar{v}/dz$ relative to the nonbreaking configured runs. At location 2 with the stack of four current meters (second from top panel, Fig. 5), the reduced shear $d\bar{v}/dz$ of the breaking configured model results in much better agreement (rms error 3 cm s^{-1}) with the vertical profile \bar{v} data (Garcez-Faria et al. 1998) than the nonbreaking configuration (rms error 11 cm s^{-1}). This further suggests that the breaking configured model is preferable.

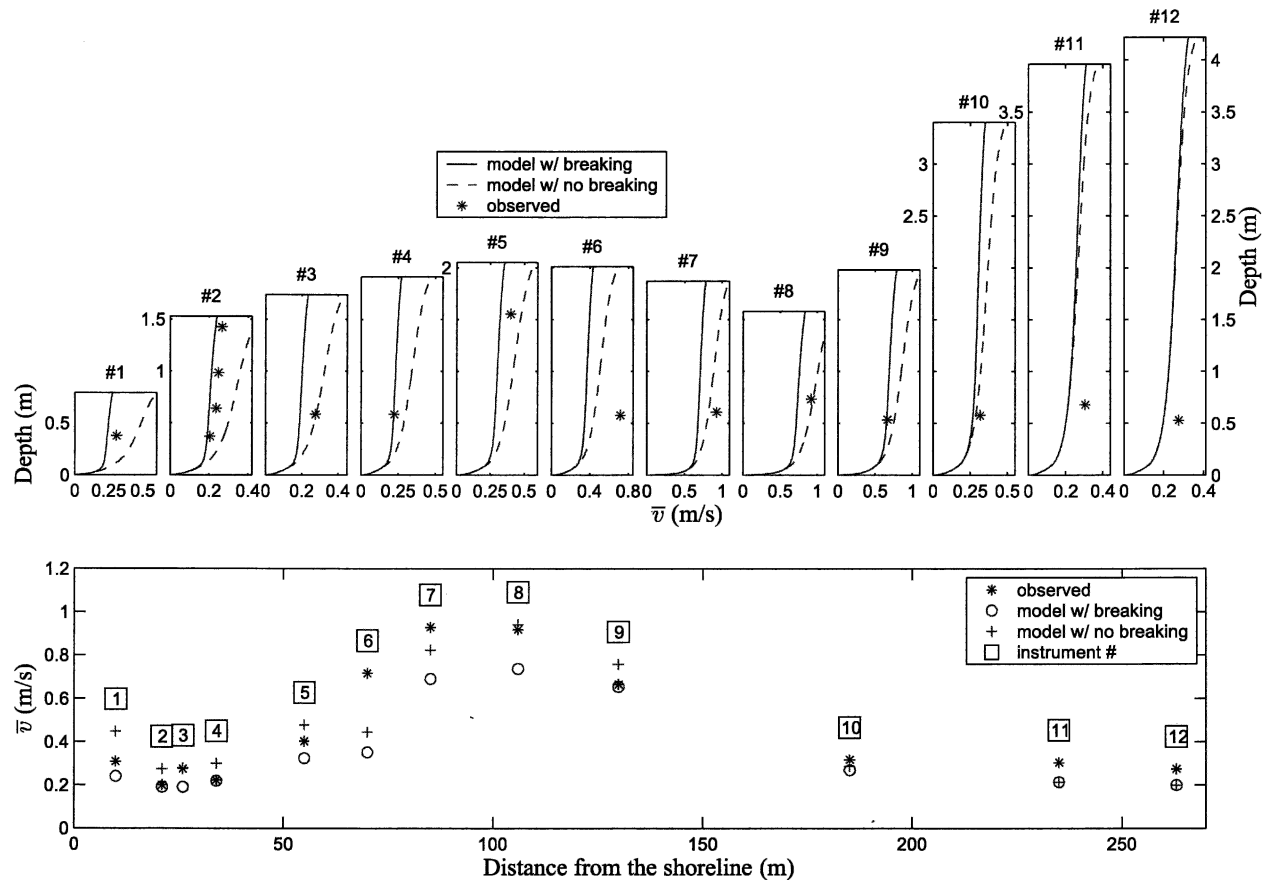


FIG. 5. (bottom) Observed \bar{v} (*) and breaking-configured (circles) and nonbreaking-configured (+) modeled \bar{v} vs distance from the shoreline. The sensor number is indicated in the square box. At location 2, the sensor closest to the bed is shown. The rms errors are 0.15 and 0.11 m s^{-1} for the breaking and nonbreaking model configurations, respectively. (top) Breaking (solid) and nonbreaking (dashed) vertical \bar{v} profiles at each numbered sensor (indicated above each panel) with the observed \bar{v} (*) at the appropriate height above the bed.

However, at location 5, also relatively high up in the water column, neither breaking nor nonbreaking is clearly preferable. The offshore locations where no wave breaking occurs (e.g., locations 11 and 12), the shear $d\bar{v}/dz$ for both configurations is the same.

6. Analysis of the Duck94 case example

Although the breaking-configured model is relatively simple and neglects much physics, the reproduction of the observed nondimensional surf-zone \bar{v} depth dependence, and the general agreement with the \bar{v} observations without the tuning of any model parameters suggests that the basic processes governing the turbulence and mean flow in the bulk of the water column are adequately represented. This allows use of the model to study the effects of wave breaking, variable water depth, and bed roughness on the mean alongshore cur-

rent, its shear, and an appropriately defined drag coefficient.

a. The effect of wave breaking on vertical shear $d\bar{v}/dz$

The vertical shear is often used to infer the bottom stress $\rho\bar{v}_*^2$ through a log-layer model, either by fitting \bar{v} observations to 1)

$$\bar{v}(z) = \frac{\bar{v}_*}{\kappa} \log(z/z_a)$$

(e.g., Garcez-Faria et al. 1998) or 2) $d\bar{v}(z)/dz = \bar{v}_*/(\kappa z)$ (Trowbridge et al. 1999; Trowbridge and Elgar 2001) where \bar{v}_* is the bed friction velocity and z_a is a wave-induced apparent roughness. The ability of the estimated $\bar{v}_*^{(\text{fit})}$ from both methods to reproduce the known \bar{v}_{*s} is tested at the 12 Duck94 case-example instrument locations.

By fitting modeled \bar{v} profiles over 25%–50% of the water column, the two log-fit methods (with very high skill, $r^2 > 0.98$) yield near-identical $\bar{v}_*^{(\text{fit})}$ at all locations in both breaking or nonbreaking configurations. Fitting higher up (e.g., 50%–75%) in the water column, yields meaningless $\bar{v}_*^{(\text{fit})}$ because of the near-surface boundary layer, highlighting the potential problem in applying the log-fit method over the entire water column even in nonwave (i.e., wind forced) environments. Hereinafter, the fits are done over 25%–50% of the water column. For the nonbreaking model configuration, the (fit to the lower water column) ratio $\bar{v}_*^{(\text{fit})}/\bar{v}_{*s} \approx 1.3$ (circles in Fig. 6), differing from one because of nonzero nondimensional shear in the stability function (appendix C). The log-fit inferred z_a are 2–12 times the bed roughness z_{ob} , consistent with the concept of a wave-enhanced apparent roughness (Grant and Madsen 1979). The breaking model configuration results in significantly reduced (by 60%) vertical shear and thus also reduced $\bar{v}_*^{(\text{fit})}$ for nondimensional wave dissipation $\bar{\epsilon}_w/(gh)^{3/2} \geq 10^{-4}$ (asterisks in Fig. 6). Wave breaking did not reduce the log-fit skill (recall $r^2 > 0.98$) in a particular manner. The reduction in $\bar{v}_*^{(\text{fit})}$ suggests that log-fit inferred c_d (via $\bar{v}_*^2/\langle|\mathbf{u}|v\rangle$) in the surf zone are biased low, potentially by $(0.4)^2$. This low bias is consistent with the Garcez-Faria et al. (1998) result that log-fit c_d decreases with increased wave breaking. For the breaking model configuration, the log-fit inferred z_a are 1/100 of z_{ob} , indicating that the concept of apparent roughness in the surf zone requires modification.

b. Testing parameterizations of drag coefficient

For both breaking and nonbreaking model configurations, c_d is inferred at the 11 Duck94 instrument locations where k_{rms} was observed (asterisks in Fig. 3e) by $c_d = \bar{v}_{*s}^2/\langle|\mathbf{u}|v\rangle$, where $\langle|\mathbf{u}|v\rangle$ is estimated from the modeled time series at the height of the instrument. The breaking model-inferred c_d range (1.3×10^{-3} – 4.3×10^{-3} , with the exception foreshore location $c_d = 6.0 \times 10^{-3}$, Fig. 7) is within the range of c_d inferred during the Duck94 and SandyDuck field experiments using cross-shore integrated momentum balance (Feddersen et al. 1998, 2003) or an inverse method (Feddersen et al. 2004). This c_d range also largely is consistent with those inferred by Garcez-Faria et al. (1998) using a log-fit method. The surf zone c_d (mean 3.8×10^{-3}) are larger than c_d seaward of the surf zone (mean 1.4×10^{-3}), consistent with the momentum balances–inferred c_d in each region (Feddersen et al. 1998) and alongshore current modeling (Ruessink et al. 2001). This contrasts the results of Chen et al. (2003) who suggest that a smaller surf-zone c_d results in improved alongshore current pre-

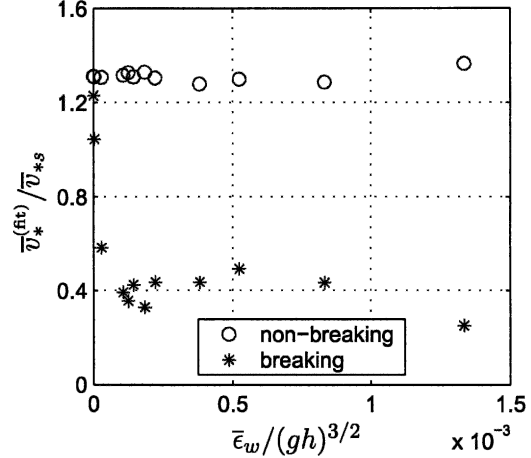


FIG. 6. The ratio $\bar{v}_*^{(\text{fit})}/\bar{v}_{*s}$ vs nondimensionalized wave dissipation $\bar{\epsilon}_w/(gh)^{3/2}$ for both breaking (asterisks) and nonbreaking (circles) model configurations.

dictions. As expected, the nonbreaking model-inferred c_d are reduced relative to the breaking c_d , except for the three locations seaward of the surf zone.

The breaking model-inferred c_d are compared with the Manning–Strickler formulation (Sleath 1984), where

$$c_d = 0.015 \left(\frac{k_{\text{rms}}}{h} \right)^{1/3}. \quad (13)$$

A close relationship between c_d and $(k_{\text{rms}}/h)^{1/3}$ is observed with correlation $r = 0.96$ and $r = 0.91$ for the breaking and nonbreaking model configurations (Fig. 7), similar to the relationship reported by Garcez-Faria

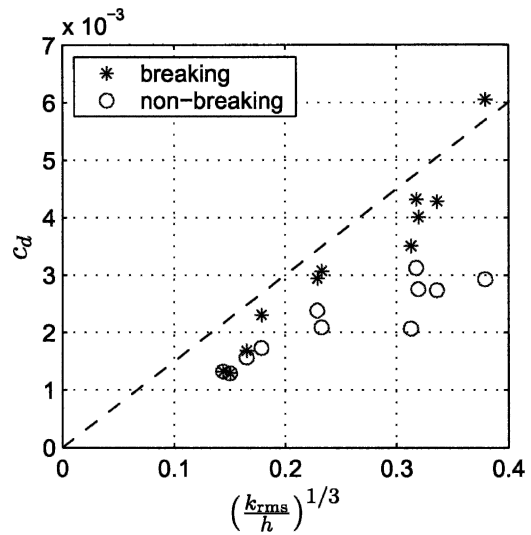


FIG. 7. The model-inferred c_d at instrument locations vs the observed $(k_{\text{rms}}/h)^{1/3}$. The dashed line is the Manning–Strickler Eq. (13). Only the 11 locations where k_{rms} was measured are included.

et al. (1998) for log-fit inferred c_d . The Manning–Strickler c_d parameterization (13) predicts well the breaking c_d (dashed line in Fig. 7) suggesting that surf-zone bed roughness is important to \bar{v} and c_d in the surf zone. However, the correlation between c_d and both $(k_{\text{rms}}/h)^{1/m}$ with $m = 1$ and $m = 2$ are also $r \geq 0.96$. There is also a high correlation between c_d and $(k_{\text{rms}}/h)^{1/3}$ using a constant k_{rms} , indicating a strong c_d dependence on water depth. The model-derived c_d and k_{rms}/h relationship contradicts the lack of an observed relationship in the surf zone between c_d (derived from momentum balances or inverse method) and k_{rms}/h (Feddersen et al. 2003, 2004).

7. Discussion

a. Effect of depth variation on \bar{v} and c_d

Factors affecting \bar{v} and c_d include the water depth, k_{rms} , orbital wave velocities, forcing, and $\bar{\epsilon}_w$, which can vary in many ways. Here the effect of h variation without wave breaking on \bar{v} and c_d is considered in isolation. A surface wind stress ($\bar{v}_{*s} = 0.014 \text{ m s}^{-1}$) is applied with fixed $k_{\text{rms}} = 2 \text{ cm}$. The depth is varied between 2 and 4 m, values representative of the nearshore region seaward of a typical surf zone. The H_{rms} is given by conserving the cross-shore energy flux (i.e., $H_{\text{rms}}^2 \sqrt{gh}$) with the 4-m depth $H_{\text{rms}} = 0.75 \text{ m}$. Thus H_{rms} and orbital wave velocities increase in shallower water.

With these conditions, at a fixed elevation (0.5 m) above the seabed, \bar{v} and the inferred c_d are relatively constant, varying by no more than 5%. Not surprisingly, the middepth (or depth-averaged) \bar{v} increases with depth from 0.81 to 1 m s^{-1} , and the middepth c_d decreases slightly (from 1.85×10^{-3} to 1.69×10^{-3}) and is fit equally well with any of h^{-m} ($m = 1, 1/2, 1/3$). Fixing a constant $H_{\text{rms}} = 0.75 \text{ m}$ and running the model with depths from 0.75 to 4 m, results in a fixed elevation (0.5 m) c_d variation from 1.9 to 2.4 ($\times 10^{-3}$). The weak c_d variation with variable h without wave breaking suggests that the strong c_d variation with h in the Duck94 case example is only indirectly due to depth variation because wave breaking increases in shallower water and turbulence penetrates a greater percentage of the water column. The effect of varying other nonbreaking parameters (wave period, angle, etc.) is understood qualitatively (e.g., Grant and Madsen 1979) and is not investigated.

b. Effect of wave breaking and bed roughness on \bar{v} and c_d

For fixed water depth, the relative effects of wave breaking and bed roughness on \bar{v} and c_d are examined.

The conditions at Duck94 location 9 ($x = 130 \text{ m}$, $h = 2 \text{ m}$) are representative of a general surf zone and \bar{v} is predicted well with the given forcing, $\bar{\epsilon}_w$, and k_{rms} (section 5). To isolate the relative effects of wave breaking versus bottom roughness, the surface stress \bar{v}_{*s}^2 (forcing) is kept fixed. However, the amount of breaking-wave energy entering the water column as turbulence is varied. The surface flux TKE boundary condition becomes

$$K_v dk/dz = \alpha \bar{\epsilon}_w T \delta(t - nT), \quad (14)$$

where α , the percentage of breaking-wave energy entering the water column, ranges between 0 and 0.5. The default value previously used is $\alpha = 0.25$. The bed roughness k_{rms} is varied between 1 and 8 cm, which spans the range of observed k_{rms} (Thornton et al. 1998; Gallagher et al. 2003; Feddersen et al. 2003). Results are examined at 0.9 m above the bed, near the midwater column, slightly above a typical measurement height, but also representative of the depth-averaged current. Aside from very near surface or near-bed vertical locations, the results do not change significantly with different vertical locations.

The resulting \bar{v} and c_d are contoured as a function of α and k_{rms} in Fig. 8. The variability of \bar{v} ($0.4\text{--}1 \text{ m s}^{-1}$) and c_d ($1.5 \times 10^{-3}\text{--}6 \times 10^{-3}$) are much greater than with depth variation alone (section 6a). The decrease in \bar{v} with increased α occurs because the increased breaking-wave turbulence decreases the shear below the measurement depth. The slope of the contour lines reveal the relative importance of an increased α or k_{rms} to the variation of \bar{v} and c_d , and over this parameter range each contributes approximately equally. For example, at $\alpha = 0.25$, varying k_{rms} results in \bar{v} between 0.5 and 0.85 m s^{-1} and c_d between 2.0 and 4.0 ($\times 10^{-3}$). At the observed $k_{\text{rms}} = 2.4 \text{ cm}$, varying α gives \bar{v} between 0.59 and 0.84 m s^{-1} and c_d between 2.0 and 3.4 ($\times 10^{-3}$). Both factors have a significant effect, contrasting previous results that found no relationship between surf zone k_{rms} and c_d (Feddersen et al. 2003, 2004). Except very close to the bed, k_{rms} has a negligible effect on the $\bar{\epsilon}$, which is dominated by α .

These results show the dependence of \bar{v} and c_d on α and k_{rms} , while the other variables remain fixed. However, if H_{rms} is variable, then $\bar{\epsilon}_w$, the surface forcing, and the orbital wave velocities change and all three affect the mean current and c_d in different ways. In along-shore uniform conditions (with narrowband waves) the wave forcing and the wave dissipation are linked through $dS_{xy}/dx = \rho \bar{\epsilon}_w (\sin \theta_0 / c_0)$ (e.g., Thornton and Guza 1986), where θ_0 and c_0 are the offshore wave angle and phase speed, respectively. At the same instrument location ($x = 130 \text{ m}$), the effect of varying

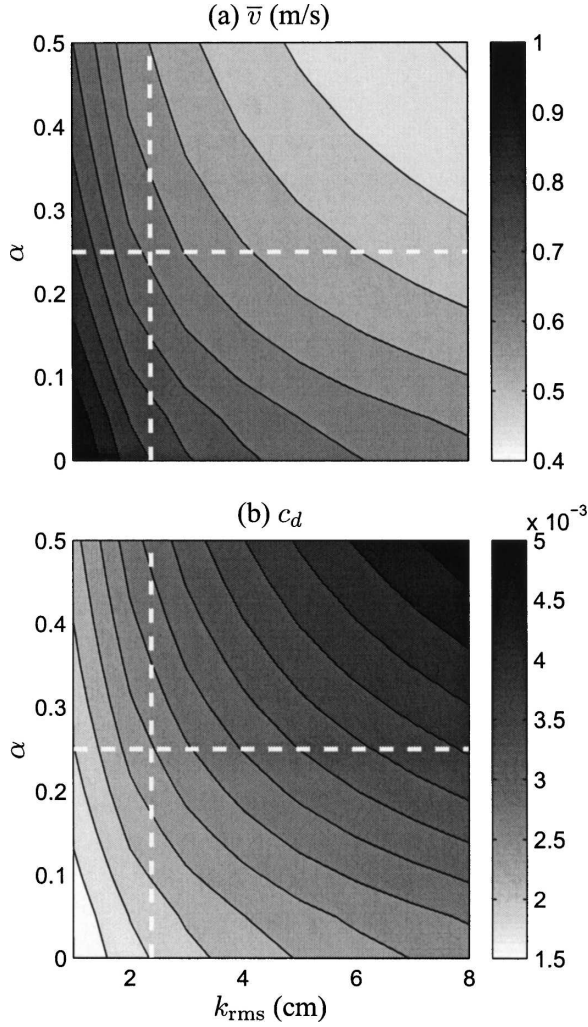


FIG. 8. Contours of (a) \bar{v} and (b) c_d at 0.9 m above the bed as a function of k_{rms} and α [(14)]. The white-dashed lines indicate the observed $k_{rms} = 2.4$ cm and the $\alpha = 0.25$ [(14)] used in section 5.

H_{rms} , and thus (through linear theory) the orbital wave velocities and (through a wave transformation model) the wave dissipation, is examined with the breaking configuration (11). The H_{rms} is varied from 0.7 to 1.5 times the original wave height $H_{rms} = 0.75$ m, resulting in $\bar{\epsilon}_w/\bar{\epsilon}_{w0}$ ($\bar{\epsilon}_{w0}$ is the original wave dissipation) ranging from 0.1 to 3.6. The modeled \bar{v} and c_d 0.9 m above the bed are presented in Fig. 9 as a function of k_{rms} and $\bar{\epsilon}_w/\bar{\epsilon}_{w0}$. The \bar{v} is a very strong function of the waves and only weakly of k_{rms} . Although increasing $\bar{\epsilon}_w/\bar{\epsilon}_{w0}$ tends to decrease the shear, the associated increased forcing causes \bar{v} to increase. The inferred c_d is (except for weak wave dissipation) almost completely a function of k_{rms} (Fig. 9b). For a fixed k_{rms} , the competing effects of wave forcing, orbital wave velocities, and breaking-wave-generated turbulence on c_d approximately bal-

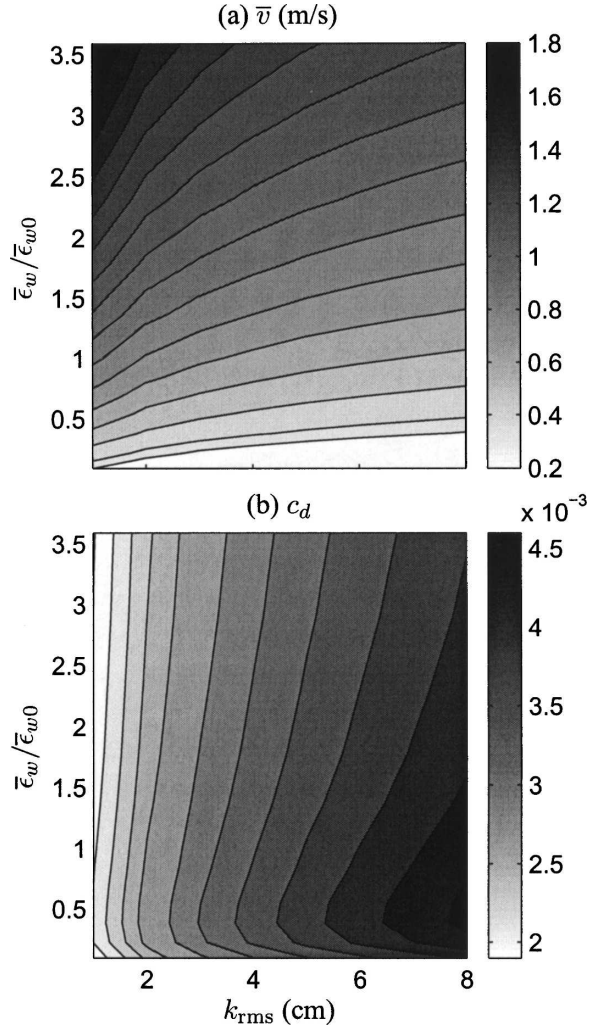


FIG. 9. Contours of (a) \bar{v} and (b) c_d at 0.9 m above the bed as a function of k_{rms} and $\bar{\epsilon}_w/\bar{\epsilon}_{w0}$.

ance. However, breaking-wave-generated turbulence cannot be neglected. Similar model runs, but with the nonbreaking configuration, result in a 30%–50% reduction in c_d , (e.g., Fig. 7). This suggests that (if α is fixed) in the fixed-depth surf zone c_d variability is dominated by k_{rms} with breaking-wave-generated turbulence setting the background level of c_d .

8. Summary

A model is described that solves for the vertical structure of the currents and turbulence in the surf zone. Breaking-wave-generated turbulence, adapted from open-ocean models, is input through a time-dependent surface flux of turbulence. Two model configurations, breaking and nonbreaking, are used to test whether the inclusion of a surface TKE flux improves

surf zone turbulence predictions. The model coefficients and closures are based on the turbulence and open ocean wave-breaking literature, and are not adjusted to optimize model–data agreement. The model is simple and neglects much physics, but it is able (without tuning) to qualitatively reproduce the existing field turbulence and mean flow observations. A constant surface mixing length $z_{0s} = 0.2$ m (Gemrich and Farmer 1999) results in better model–data agreement than the fixed ratio z_{0s}/H_{rms} typically used in open-ocean turbulence modeling. The reason for this is not understood, and an improved understanding of the factors influencing z_{0s} is needed.

The most energetic breaking-wave observations of Trowbridge and Elgar (2001) are generally reproduced with both the breaking and nonbreaking model configurations. This is because the (near bed) observed turbulence is dominated by near-bed processes. The mean dissipation and production are well (factor of 2) predicted, and the mean alongshore current is somewhat underpredicted. This may be because the specified inputs (i.e., wave forcing or bed roughness) are in error or the model simply could be too frictional. Because of the relative deep instrument location, neither the breaking or nonbreaking model configurations is preferable. Because the instrument location is near the bed where shear production is large, the excess dissipation observed under open-ocean breaking waves is not present.

The second case example from the Duck94 field experiment has only mean alongshore current measurements. Thus historical surf-zone dissipation observations are used to test the model. A nondimensionalization for surf zone dissipation is developed that collapses the different datasets and suggests that a significant fraction of the wave energy dissipation was observed. With the breaking configuration, the modeled nondimensional dissipation profiles overlap the observations, whereas the nonbreaking model configuration does not (Fig. 4). The mean alongshore current observations are generally reproduced, although both model configurations appear too frictional (i.e., an underprediction bias). At one location with vertical profile data, the breaking model configuration results in much improved alongshore current predictions. Based on the case examples, the breaking model configuration is preferred for the surf zone. Wave breaking decreases (around 60%) the vertical shear of the modeled alongshore current (Fig. 5), indicating that the bottom stress inferred through log-profile fits is biased low. The model-inferred drag coefficient c_d is larger in the surf zone, and is well predicted by the Manning–Strickler Eq. (13). This contrasts with previous results that have

shown no c_d dependence on k_{rms}/h (Feddersen et al. 2003, 2004).

In isolation, variable water depth does not have a large effect on the mean alongshore current or drag coefficient, suggesting that the c_d depth-dependence is indirect. For a fixed water depth (2 m), variable bed roughness k_{rms} and variable percentage of wave energy entering the water column have a much larger effect on \bar{v} and c_d (0.9 m above the bed) than depth variation alone, and contribute approximately equally to \bar{v} and c_d . In contrast, by covarying the wave height, wave dissipation, and wave forcing, and varying k_{rms} separately, \bar{v} is only weakly dependent on k_{rms} but c_d is almost completely a function of k_{rms} . This is because, as the wave dissipation increases, so does the forcing and orbital wave velocities, which, according to the model, conspire to keep c_d approximately constant.

Acknowledgments. This work was funded by NSF, ONR, and NOPP. Karin Bryan graciously provided her dissipation data. Steve Elgar, Bob Guza, Tom Herbers, Britt Raubenheimer, and staff from Scripps Institution of Oceanography collected the fixed Duck94 current-meter data. Workers E. B. Thornton and T. P. Stanton and staff from the Naval Postgraduate School collected and provided the Duck94 vertical profile data. The Field Research Facility, Coastal Engineering Research Center, Duck, North Carolina, provided the bathymetric surveys and 8-m-depth wave data. Gene Terray, Bob Guza, Steve Henderson, and two anonymous reviewers provided valuable feedback.

APPENDIX A

The Depth Dependence of the Mean Wave Forcing

The depth dependence of the alongshore wave forcing in the surf zone is not well understood and as of yet there is no consensus on how it should be applied. For example, Deigaard (1993) argues that for a flat bottom and a surface wave roller, the mean alongshore wave forcing acts as a surface stress. Others have used a combination of a depth-uniform body force and surface stress for the surf zone alongshore forcing (Reniers et al. 2004). Using a wave-following coordinate transformation, Mellor (2003) derived the depth-dependence of the radiation stress terms but did not explicitly consider wave breaking or surface wave rollers. The concept of a Stokes-drift-induced vortex force (Craik and Leibovich 1976) leading to depth-dependent mean wave forcing term has been discussed in the context of global ocean (McWilliams and Restrepo 1999) and shelf cir-

ulation (McWilliams et al. 2004), respectively, and could potentially be applied in the surf zone.

All model experiments in sections 3–6 were run with the mean alongshore wave forcing applied as a surface stress (5). All of these experiments were also run with a depth-uniform body force for the mean alongshore wave forcing \bar{F}_y [i.e., $\bar{F}_y = -(hp)^{-1}dS_{yx}/dx$]. These two forcing choices are the end limits of the various depth-dependence possibilities. For the model–data comparisons in sections 3 and 4, the surface-stress-forced runs were $< 2 \text{ cm s}^{-1}$ larger than the body-forced runs at the height above the bed of the instrument. In terms of model data agreement, neither forcing choice is clearly preferable. For all runs, the surface stress forcing resulted in a 2%–12% larger surface \bar{v} relative to the uniform body forcing. Between the two forcings there was insignificant differences in the TKE dynamics. The conclusions drawn in sections 5 and 6 do not depend on the forcing choice. Given the relatively small differences in the model results with the two forcings, the explicit surf zone approach of Deigaard (1993) is followed.

There are also significant uncertainties in the depth dependence of the mean cross-shore wave forcing. Uncertainties also exist in the choice of boundary conditions for u and/or cross-shore mass flux constraints to apply in a 1D model situation. To avoid these uncertainties, mean cross-shore forcing is not included. This may change somewhat the turbulence (i.e., increased shear production) and increase vertical mixing, but is unlikely to affect the breaking-wave-generated turbulence results here.

APPENDIX B

Steady versus Time-Dependent TKE Surface Flux

Whether the model surface TKE flux boundary condition is steady [(10)] (e.g., Craig and Banner 1994; Burchard 2001) or time varying [(11)] the result is different turbulence and mean flow solutions. This is illustrated with idealized model simulations representative of open-ocean breaking conditions using both time-dependent [(11)] and steady [(10)] surface TKE flux boundary conditions. The conditions are depth of 20 m, a wind friction velocity of $\bar{u}_* = 0.02 \text{ m s}^{-1}$, and (following Craig and Banner 1994; Burchard 2001) the wave dissipation is a function of the wind friction velocity; that is, $\bar{\epsilon}_w = 100\bar{u}_*^3$. The surface mixing length of $z_{0s} = 0.2 \text{ m}$ (Gemmrich and Farmer 1999) is used. The period of breaking is varied between $T_{br} = 5 \text{ s}$, and $T_{br} = 60 \text{ s}$. Breaking periods of 5–15 s are typical in the surf zone, and the T_{br} of 30–60 s are representative of the

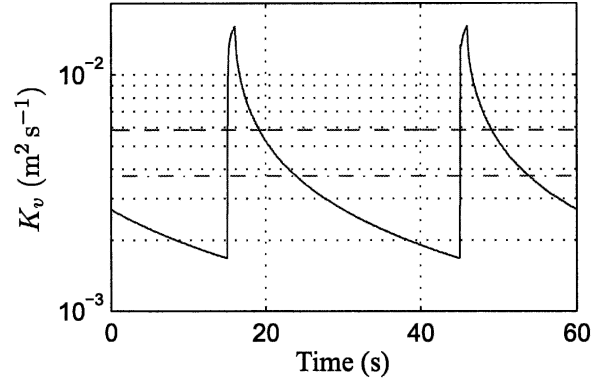


FIG. B1. Plot of K_v vs time for the time-dependent (solid) and steady (dashed) surface TKE flux. The period of wave breaking is $T_{br} = 30 \text{ s}$. The dash-dot curve is the (time-averaged) \bar{K}_v with the time-dependent surface TKE flux.

time interval between breaking in the intermediate water depths (Babanin et al. 2001). The model is run for various T_{br} until equilibrium is reached. In addition a passive tracer θ is added to the model, which evolves according to

$$\frac{\partial \theta}{\partial t} = \frac{\partial}{\partial z} \left(K_v \frac{\partial \theta}{\partial z} \right)$$

with no-flux bottom boundary condition and an initial condition of zero concentration everywhere. After model equilibrium is reached, a surface boundary condition of $\theta = 1$ is applied and data is taken from 3–5 min after boundary condition application. Because the θ dynamics are linear the value of the surface boundary condition is arbitrary, and only a few breaking periods are examined for vertical concentration fluxes because the equilibrium solution ($\theta = 1$ everywhere) will be reached for all T_{br} .

The time-dependent surface TKE-flux boundary condition results in time dependence in all the variables and, because the equations are nonlinear, the mean (time averaged) solutions are dependent upon T_{br} . This is illustrated with the modeled near-surface K_v (Fig. B1) with $T_{br} = 30 \text{ s}$ and the steady surface TKE flux boundary condition. With $T_{br} = 30 \text{ s}$ (solid curve), K_v varies an order of magnitude between 0.002 and $0.02 \text{ m}^2 \text{ s}^{-1}$, and the time-averaged $\bar{K}_v = 3.7 \times 10^{-3} \text{ m}^2 \text{ s}^{-1}$ (dash-dot curve). With the steady boundary condition, $K_v = 5.9 \times 10^{-3} \text{ m}^2 \text{ s}^{-1}$ (dashed curve) and the ratio of mean K_v with the two boundary conditions is 0.63. This ratio depends upon T_{br} . For example, 1 m below the surface, the ratio of the mean K_v with the time-dependent and steady surface TKE flux boundary conditions decreases with increasing T_{br} (diamonds in Fig. B2).

A similar T_{br} dependence exists for other turbulent

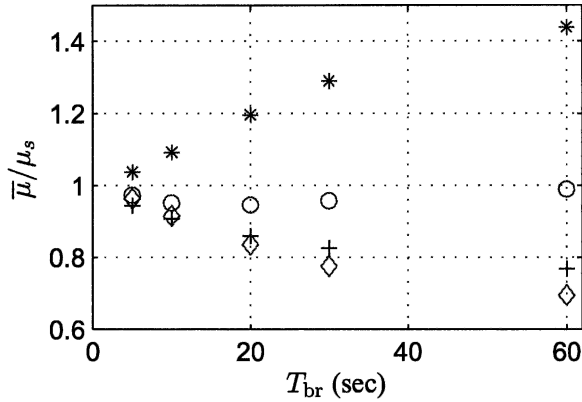


FIG. B2. Ratio of time-dependent TKE surface-flux [(11)] derived $\bar{\mu}$ to steady [(10)] TKE surface-flux derived μ_s 1 m below the surface vs breaking period T_{br} , where $\bar{\mu}$ represents the (mean) $d\bar{u}/dz$ (asterisks), tracer flux (pluses), $\bar{\epsilon}$ (circles), and \bar{K}_v (diamonds).

and mean flow quantities (Fig. B2). One meter below the surface, the ratio of the mean shear $d\bar{u}/dz$ with time-dependent to steady surface TKE flux increases with increasing T_{br} (asterisks in Fig. B2), resulting in a 40% increase in shear relative to the steady boundary condition. The mean dissipation ratio is only weakly affected by variable T_{br} (circles in Fig. B2), but the mean vertical tracer flux $-\langle K_v d\theta/dz \rangle$ is strongly dependent upon T_{br} (pluses in Fig. B2). This illustrates the potential dependence of heat and gas fluxes through the surface breaking layer on the frequency of wave breaking, and the potential pitfall in using the steady surface TKE flux boundary condition in mixed layer modeling. In addition, in the open ocean, the interval between breaking-wave events T_{br} can also be considerably longer than 60 s.

APPENDIX C

Effect of the Stability Function on Shear

In their paper, Canuto et al. (2001) state that as the Richardson number approaches zero (i.e., no stratification), that “to first order in shear” (α_M), $C_\mu^4 = 0.107$ as expected in a log layer. However it is interesting to note that in a log layer the shear is nonnegligible, and thus use of the Canuto stability function (8) results in turbulence, dissipation, and shear that deviates slightly from a traditional log layer. To demonstrate this, consider a loglike layer where production equals dissipation, which results in

$$\frac{P}{\epsilon} = \frac{K_v S^2}{\epsilon} = \frac{C_\mu^4 k^2 S^2}{\epsilon^2} = C_\mu^4 \alpha_M = 1. \quad (C1)$$

Using (8), (C1) is solved for the nondimensional shear giving $\alpha_M = 13$ and $C_\mu^4 = 0.077$, a reduction over the zero shear $(C_\mu^0)^4 = 0.107$ and resulting in larger shear. This is heuristically demonstrated by using $k = \bar{v}_*^2 / C_\mu^2$, assuming $l = \kappa z$, and the relationship for ϵ to show that

$$13 = \alpha_M = \frac{C_\mu^2}{(C_\mu^0)^6} \frac{(\kappa z)^2}{\bar{v}_*^2} \left(\frac{d\bar{v}}{dz} \right)^2,$$

which results in

$$\frac{d\bar{v}}{dz} = \frac{\sqrt{13(C_\mu^0)^3 \bar{v}_*}}{C_\mu} \frac{\bar{v}_*}{\kappa z} = 1.28 \frac{\bar{v}_*}{\kappa z},$$

which is close to the ratio $\bar{v}_*^{(fit)}/\bar{v}_{*s} \approx 1.3$ for the non-breaking model configuration (Fig. 6).

REFERENCES

- Agrawal, Y. C., E. A. Terray, M. A. Donelan, P. A. Hwang, A. J. Williams, W. Drennan, K. Kahm, and S. Kitaigorodskii, 1992: Enhanced dissipation of kinetic energy beneath breaking waves. *Nature*, **359**, 219–220.
- Anis, A., and J. N. Moum, 1995: Surface wave–turbulence interactions: Scaling $\epsilon(z)$ near the sea surface. *J. Phys. Oceanogr.*, **25**, 2025–2045.
- Babanin, A. V., I. R. Young, and M. L. Banner, 2001: Breaking probabilities for dominant surface waves on water of finite constant depth. *J. Geophys. Res.*, **106**, 11 659–11 676.
- Bryan, K. R., K. P. Black, and R. M. Gorman, 2003: Spectral estimates of dissipation rate within and near the surf zone. *J. Phys. Oceanogr.*, **33**, 979–993.
- Burchard, H., 2001: Simulating the wave-enhanced layer under breaking surface waves with two-equation turbulence models. *J. Phys. Oceanogr.*, **31**, 3133–3145.
- Canuto, V. M., A. Howard, Y. Cheng, and M. S. Dubovikov, 2001: Ocean turbulence. Part I: One-point closure model—Momentum and heat vertical diffusivities. *J. Phys. Oceanogr.*, **31**, 1413–1426.
- Church, J. C., and E. B. Thornton, 1993: Effects of breaking wave induced turbulence within a longshore current model. *Coastal Eng.*, **20**, 1–28.
- Chen, Q., J. T. Kirby, R. A. Dalrymple, F. Shi, and E. B. Thornton, 2003: Boussinesq modeling of longshore currents. *J. Geophys. Res.*, **108**, 3362, doi:10.1029/2002JC001308.
- Cox, D. T., and N. Kobayashi, 2000: Identification of intense, intermittent coherent motions under shoaling and breaking waves. *J. Geophys. Res.*, **105**, 14 223–14 236.
- Craig, P. D., 1996: Velocity profiles and surface roughness under breaking waves. *J. Geophys. Res.*, **101**, 1265–1277.
- , and M. L. Banner, 1994: Modeling wave-enhanced turbulence in the ocean surface layer. *J. Phys. Oceanogr.*, **24**, 2546–2559.
- Craik, A. D. D., and S. Leibovich, 1976: A rational model for Langmuir circulations. *J. Fluid Mech.*, **73**, 401–426.
- Deigaard, R., 1993: A note on the three-dimensional shear stress distribution in a surfzone. *Coastal Eng.*, **20**, 156–171.
- Drennan, W. M., M. A. Donelan, E. A. Terray, and K. B. Katsaros, 1996: Oceanic turbulence dissipation measurements in SWADE. *J. Phys. Oceanogr.*, **26**, 808–815.
- Duncan, J. H., 1981: An experimental investigation of breaking

- waves produced by a towed hydrofoil. *Proc. Roy. Soc. London*, **377A**, 331–348.
- Elgar, S., R. T. Guza, B. Raubenheimer, T. H. C. Herbers, and E. Gallagher, 1997: Spectral evolution of shoaling and breaking waves on a barred beach. *J. Geophys. Res.*, **102**, 15 797–15 805.
- Feddersen, F., R. T. Guza, S. Elgar, and T. H. C. Herbers, 1998: Alongshore momentum balances in the nearshore. *J. Geophys. Res.*, **103**, 15 667–15 676.
- , E. L. Gallagher, S. Elgar, and R. T. Guza, 2003: The drag coefficient, bottom roughness, and wave-breaking in the nearshore. *Coastal Eng.*, **48**, 189–195.
- , R. T. Guza, and S. Elgar, 2004: Inverse modeling of one-dimensional setup and alongshore current in the nearshore. *J. Phys. Oceanogr.*, **34**, 920–933.
- Fredsoe, J., and R. Deigaard, 1992: *Mechanics of Coastal Sediment Transport*. World Science, 369 pp.
- , B. M. Sumer, A. Kozakiewicz, L. H. C. Chua, and R. Deigaard, 2003: Effect of externally generated turbulence on wave boundary layer. *Coastal Eng.*, **49**, 155–183.
- Gallagher, E. L., S. Elgar, and E. B. Thornton, 1998: Megaripple migration in a natural surf zone. *Nature*, **394**, 165–168.
- , E. B. Thornton, and T. P. Stanton, 2003: Sand bed roughness in the nearshore. *J. Geophys. Res.*, **108**, 3039, doi:10.1029/2001JC001081.
- Garcez-Faria, A. F., E. B. Thornton, T. P. Stanton, C. M. Soares, and T. C. Lippmann, 1998: Vertical profiles of longshore currents and related bed shear stress and bottom roughness. *J. Geophys. Res.*, **103**, 3217–3232.
- Gemmrich, J. R., and D. M. Farmer, 1999: Near-surface turbulence and thermal structure in a wind-driven sea. *J. Phys. Oceanogr.*, **29**, 480–499.
- George, R., R. E. Flick, and R. T. Guza, 1994: Observations of turbulence in the surf zone. *J. Geophys. Res.*, **99**, 801–810.
- Grant, W. D., and O. S. Madsen, 1979: Combined wave and current interaction with a rough bottom. *J. Geophys. Res.*, **84**, 1797–1808.
- Kitaigorodskii, S. A., M. A. Donelan, J. L. Lumley, and E. A. Terray, 1983: Wave turbulence interactions in the upper ocean. Part II: Statistical characteristics of wave and turbulent components of the random velocity field in the marine surface layer. *J. Phys. Oceanogr.*, **13**, 1988–1999.
- Lamarre, E., and W. K. Melville, 1991: Air entrainment and dissipation in breaking waves. *Nature*, **351**, 469–472.
- McWilliams, J. C., and J. M. Restrepo, 1999: The wave-driven ocean circulation. *J. Phys. Oceanogr.*, **29**, 2523–2540.
- , J. M. Restrepo, and E. M. Lane, 2004: An asymptotic theory for the interaction of waves and currents in coastal waters. *J. Fluid Mech.*, **511**, 135–178.
- Mellor, G. L., 2003: The three-dimensional current and surface wave equations. *J. Phys. Oceanogr.*, **33**, 1978–1989.
- , and T. Yamada, 1982: Development of a turbulence closure model for geophysical fluid problems. *Rev. Geophys.*, **20**, 851–875.
- Melville, W. K., F. Veron, and C. J. White, 2002: The velocity field under breaking waves: Coherent structures and turbulence. *J. Fluid Mech.*, **454**, 203–233.
- Mohamed, M. S., and J. C. Larue, 1990: The decay power law in grid-generated turbulence. *J. Fluid Mech.*, **219**, 195–214.
- Nikuradse, J., 1933: Stromungsgestze in glatten und rauhen rohren. *Work Rep.*, **VD1**, 361.
- Rapp, R. J., and W. K. Melville, 1990: Laboratory measurements of deep-water breaking waves. *Philos. Trans Roy. Soc. London*, **331A**, 735–800.
- Raubenheimer, B., R. T. Guza, and S. Elgar, 1996: Wave transformation across the inner surf zone. *J. Geophys. Res.*, **101**, 25 589–25 597.
- Reniers, A. J. H. M., E. B. Thornton, T. P. Stanton, and J. A. Roelvink, 2004: Vertical flow structure during SandyDuck: Observations and modeling. *Coastal Eng.*, **51**, 237–260.
- Reynolds, W. C., 1976: Computation of turbulent flow. *Annu. Rev. Fluid Mech.*, **8**, 183–207.
- Rodi, W., 1987: Examples of calculation methods for flow and mixing in stratified fluid. *J. Geophys. Res.*, **92**, 5305–5328.
- Ruessink, B. G., J. R. Miles, F. Feddersen, R. T. Guza, and S. Elgar, 2001: Modeling the alongshore current on barred beaches. *J. Geophys. Res.*, **106**, 22 451–22 463.
- Sleath, J. F. A., 1984: *Sea Bed Mechanics*. John Wiley and Sons, 335 pp.
- Svendsen, I. A., 1984: Wave heights and set-up in a surf zone. *Coastal Eng.*, **8**, 303–329.
- Tennekes, H., 1989: Two- and three dimensional turbulence. *Lecture Notes in Turbulence*, J. R. Herring and J. C. McWilliams, Eds., World Scientific, 371 pp.
- Terray, E. A., M. A. Donelan, Y. C. Agrawal, W. M. Drennan, K. K. Kahma, A. J. Williams, and P. Hwang, 1996: Estimates of kinetic energy dissipation under breaking waves. *J. Phys. Oceanogr.*, **26**, 792–807.
- , W. M. Drennan, and M. A. Donelan, 1999: The vertical structure of shear and dissipation in the ocean surface layer. *Proc. Symp. on the Wind-Driven Air-Sea Interface-Electromagnetic and Acoustic Sensing, Wave Dynamics and Turbulent Fluxes*, Sydney, Australia, University of New South Wales, 239–245.
- Thornton, E. B., and R. T. Guza, 1983: Transformations of wave height distribution. *J. Geophys. Res.*, **88**, 5925–5938.
- , and —, 1986: Surf zone longshore currents and random waves: Field data and models. *J. Phys. Oceanogr.*, **16**, 1165–1178.
- , J. L. Swayne, and J. R. Dingler, 1998: Small-scale morphology across the surf zone. *Mar. Geol.*, **145**, 173–196.
- Trowbridge, J. H., and S. Elgar, 2001: Turbulence measurements in the surf zone. *J. Phys. Oceanogr.*, **31**, 2403–2417.
- , W. R. Geyer, M. M. Bowen, and A. J. Williams, 1999: Near-bottom turbulence measurements in a partially mixed estuary: Turbulent energy balance, velocity structure, and along-channel momentum balance. *J. Phys. Oceanogr.*, **29**, 3056–3072.
- Umlauf, L., and H. Burchard, 2003: A generic length-scale equation for geophysical turbulence models. *J. Mar. Res.*, **61**, 235–265.
- Voulgaris, G., and M. B. Collins, 2000: Sediment resuspension on beaches: Response to breaking waves. *Mar. Geol.*, **167**, 167–197.